Chapter 6

Magnetic depth profile across the first-order phase transition in Dy films

Up to this chapter, this dissertation had its focus on depth-integrated information, and an profile of the magnetic structure could be obtained only by modeling of the reflectivity curves. We have seen that many thin-film properties deviate from those of the respective bulk material either due to the reduced dimension or due to interface effects like strain, lattice relaxation at interfaces and surfaces, or the increasing importance of the surface- and interface-electronic properties. Since thin magnetic layers are functional parts in many devices like storage media or GMR sensors, a knowledge of the exact magnetization profile at the respective interfaces is crucial for a proper understanding of the system properties. Consequently, there have been many efforts to obtain spatially-resolved information about magnetic structures and domains. Lateral resolution can be achieved by a variety of microscopic techniques like scanning tunneling microscopy (STM), magnetic force microscopy (MFM), Lorentz microscopy, spin-polarized low energy electron microscopy (SPLEEM), and scanning near-field optical microscopy (SNOM) with magnetic contrast [141]. While these techniques are sensitive to the layers of FM domains (and to a limited extent to AFM domains), AFM domains were mainly studied by x-ray diffraction using a focusing optic to get lateral resolution [142].

Besides lateral information, it is highly desirable to get depth-resolved information on the magnetic structure. This can be obtained from spin-polarized neutron reflectivity measurements [143, 144]. This method does not vary the probing depth and requires detailed model calculations to allow an extraction of the laterally-averaged magnetization profiles. In-plane information on the magnetic structure with a certain depth resolution can be achieved by birefringent in-plane Bragg diffraction of evanescent neutron states below the angle of total reflection [145–147]. The minimum escape depth of evanescent neutrons, and thus the depth resolution, is of the order of 100 Å. In general, however, the limits of surface-sensitive neutron scattering are posed by the low scattering intensity and the modest depth sensitivity [146]. Magnetic contributions to multilayer diffraction peaks in

resonant magnetic x-ray scattering have been used to obtain a profile of the spin polarization within a single layer, averaged over the whole multilayer structure [148, 149]. This method, however, makes use of the periodic arrangement of the interfaces and is difficult to apply to a single, chemically homogeneous medium.

This chapter reports on a novel possibility to use resonant magnetic x-ray scattering to study the magnetic depth profiles in an AFM film directly. This technique makes use of the strong change of the photon mean-free path at resonance, which provides the opportunity to tune the probing depth in a well-defined way across the sample. The potential of this technique is demonstrated for thin Dy films grown on W(110), which are particularly suited and well-defined systems exhibiting both FM and AFM phases separated by a first-order phase transition (see chapter 1). Unlike in bulk Dy, this phase transition turns out to be delayed in Dy/W(110), and is characterized by a gradually growing helical AFM domain. The growth of this domain can be determined by temperature-dependent magnetic depth profiles. The new method is based on the exact knowledge of the optical parameters across the resonance. These can be determined from reflectivity curves as demonstrated in chapter 4 for the case of Ho. The same treatment will be applied now to the case of Dy metal.

6.1 Optical parameters at the Dy M_V threshold

The optical parameters of Dy on resonance were obtained from specular-reflectivity scans recorded from a 180-ML Dy/W(110) film at 100 K, i.e. in a state, where the helical AFM structure is fully developed. Figure 6.1 shows scans in the region of the (000+τ) magnetic satellite. The analysis of the spectra was carried out in the same way and using the same model as in case of Ho, i.e. by describing the spectra as a superposition of a charge-scattering background and a magnetic satellite in a dynamical treatment (see chapter 4). Examples of the results of the least-squares fit analyses are displayed as solid lines through the data points in figure 6.1. The dotted and dashed subspectra represent the charge-scattering and the magnetic-scattering contributions, respectively. Like in case of Ho, the optical parameters could be obtained directly from the fits without any further adjustable parameters. The resulting values for β and δ are shown in figure 6.2 (b). The corresponding x-ray absorption signal (XAS) across the resonance, as obtained from the sample drain current, is shown in panel (a). For a test of consistency, the XAS and the corresponding dispersive part calculated from the XAS via Kramers-Kronig transformation, are scaled to the optical parameters (lines in panel (b)). Both show a good agreement with the behavior of the parameters obtained from the reflectivity scans. The maximum value of the absorptive part, β, is slightly larger than for Ho. Its variation across the resonance corresponds to a variation of the average absorption length, $l_{abs} = \lambda/4\pi\beta$, and thus to an information depth along the surface normal between 240 Å at 1305 eV and only 17 Å at the resonance maximum (at 1292 eV). This strong variation of the photon absorption and thus of the photon penetration depth will be used in the following to obtain the magnetic depth profile.

Like in case of Ho, also magnetic scattering from Dy shows a huge resonant enhancement

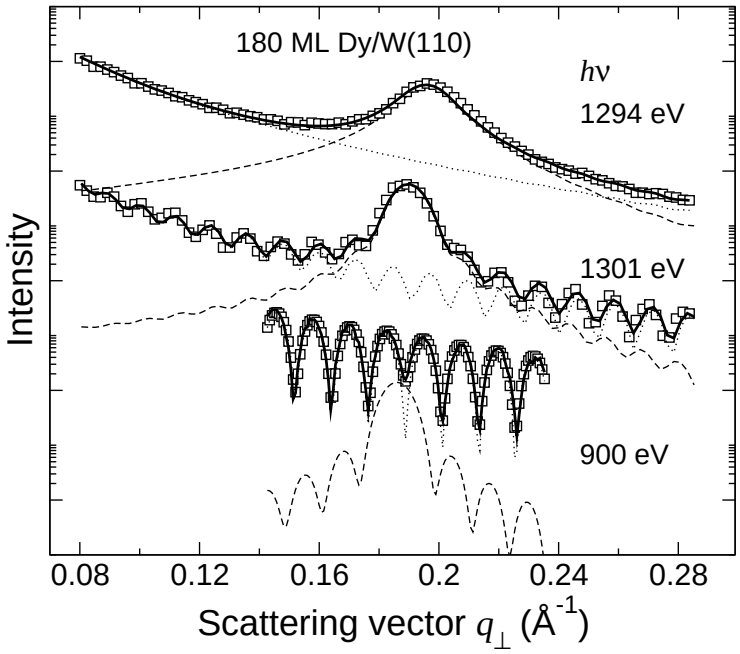

Figure 6.1: Specular x-ray reflectivity scans of a 180-ML Dy film at various photon energies across the Dy M_V absorption threshold. The solid lines through the spectra represent the results of least-squares fit analyses using the model described in chapter 4. The subspectra represent the contributions of magnetic scattering (dashed) and charge scattering (dotted).

across the M_V absorption threshold. Figure 6.2 (c) displays the integrated satellite intensity normalized to that recorded off resonance at 900 eV. An absorption correction was applied as in the Ho case. The enhancement is more than six orders of magnitude and thus slightly larger than the enhancement found for Ho at the M_V threshold. Possible reasons are the higher spin polarization and the larger number of excitation channels into the less-filled $4f$ shell in Dy.

6.2 First-order phase transition in Dy/W(110)

First-order phase transitions are difficult to understand on a microscopic scale because the physical properties of the two involved phases are usually quite different. The entropy difference between the two phases is sufficiently large in most cases to preclude statistical fluctuations in each phase close to the phase boundary, which might give short-lived regions of the respective other phase. Therefore, the phase transition has to take place by nucleation of the second phase at some special points, such as impurities or boundaries [123]. Such a nucleation is followed by the growth of regions of the second phase. As discussed in section 1.1, bulk Dy exhibits two different magnetically ordered phases, a FM and a helical AFM phase, separated by a first-order phase transition. In thin films and multilayers, this

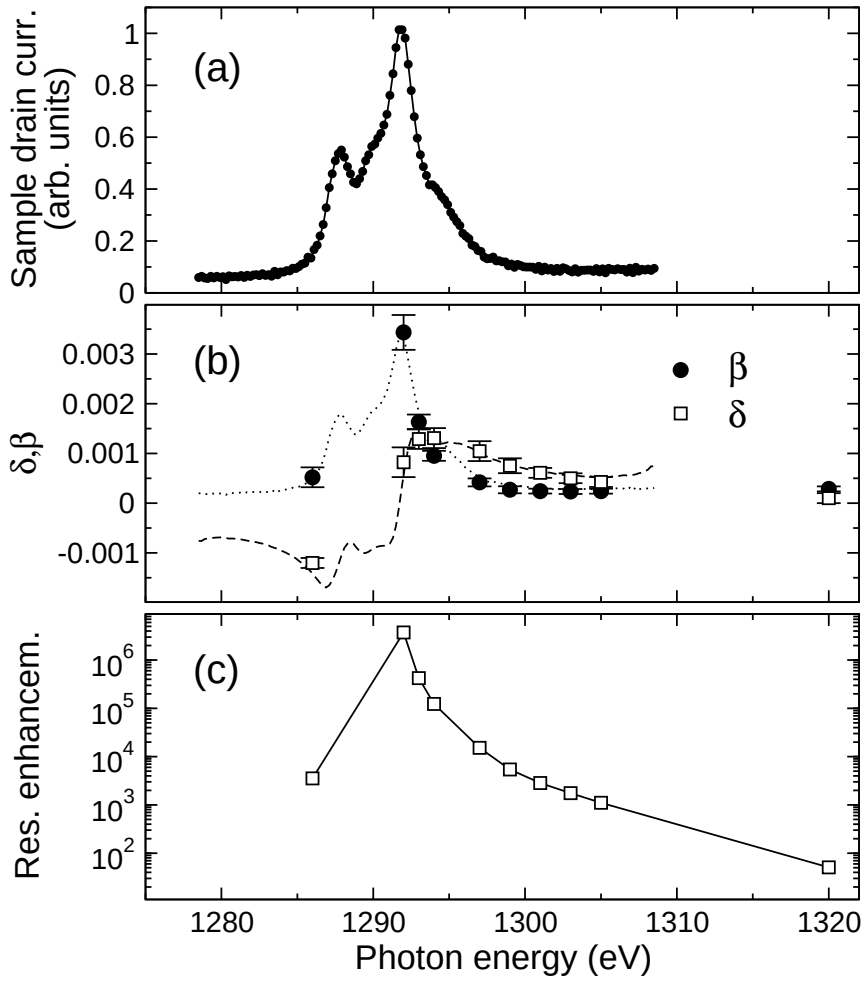

Figure 6.2: (a) XAS spectrum as recorded from the sample drain current from a 180-ML Dy film as a function of photon energy. (b) Optical parameters of Dy across the M_V absorption threshold as obtained from fit analyses exemplarily shown in figure 6.1. (c) Resonant enhancement of the integrated satellite intensity with respect to the integrated intensity measured off resonance at a photon energy of 900 eV.

phase transition can be strongly influenced by the boundaries. The influence of strain has been studied in detail for Dy-metal films embedded between layers of Y_xLu_{1-x} [150]. By choice of the Y/Lu ratio, either compressive or expansive strain can be applied to the Dy film and by that the Curie temperature, T_C, can be reduced or increased smoothly over a wide temperature range, persisting the spontaneous first-order character of the phase transition. Up to now, the influence of strain on these films was always studied in systems with two identical boundary layers [96,150,151]. This chapter deals with a phase transition in epitaxially grown Dy films on W(110). This system with inequivalent boundaries turns out to behave distinctly different from the symmetric systems studied so far.

In order to characterize the system and the phase transition, first experiments were

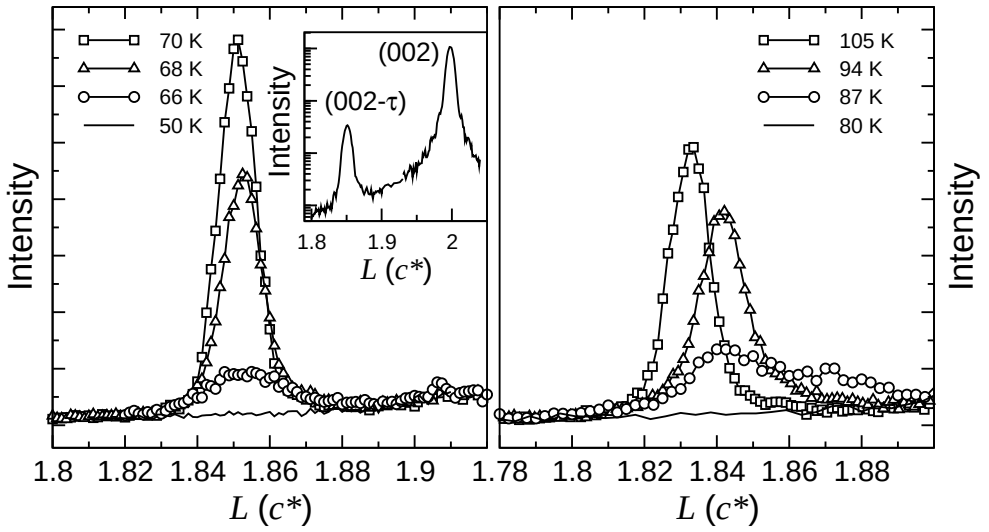

Figure 6.3: (002−τ) magnetic satellite of a 184-ML Dy film grown on W(110) across the first-order phase transition. Left panel: spectra recorded at various temperatures during cooling down. Right panel: spectra recorded while warming up. The inset displays the Dy(002) Bragg peak and the (002−τ) superstructure satellite with maximum intensity at 70 K on the cooling path.

carried out in the conventional x-ray region, where both the crystalline and the magnetic structure can be studied, the former from the (002) Bragg-peak position and the latter from the behavior of the (002−τ) superstructure reflection (see inset in figure 6.3). Spectra of the magnetic-superstructure satellite obtained from a 184-ML Dy film grown on W(110) across the first-order phase transition are displayed in figure 6.3. The data were recorded at the L_{III} resonance with a photon energy of 7780 eV using the (006) reflection of a graphite analyzer crystal to suppress the otherwise dominating charge scattering contribution (see figure 2.7). The left panel displays spectra recorded upon cooling during the phase transition from the AFM to the FM phase. The phase transition is indicated by a decreasing satellite intensity connected with the disappearance of the AFM order. The right panel shows the spectra recorded upon heating from the FM to the AFM phase. While upon cooling, the satellite is most intense at 70 K, it has not even reappeared when the sample is heated to 80 K; this clearly shows the hysteretic character of the phase transition. Information about details of the magnetic structure can be obtained from the intensity, width, and position of the magnetic satellite and - because of magneto-elastic coupling - also from the Bragg-peak position of the crystalline lattice. The results of the analysis are summarized in figure 6.4. First, we concentrate on the two upper curves, (a) the $c-$axis lattice parameter obtained from the (002) Bragg peak position and (b) the integrated intensity of the (002−τ) magnetic satellite. As expected for a first-order phase transition, the data reveal a pronounced hysteresis of both the $c-$axis parameter and the integrated satellite intensity. The $c-$axis parameter shows the characteristic expansion upon cooling (open symbols) into the FM phase (compare to figure 1.2), while the intensity of the

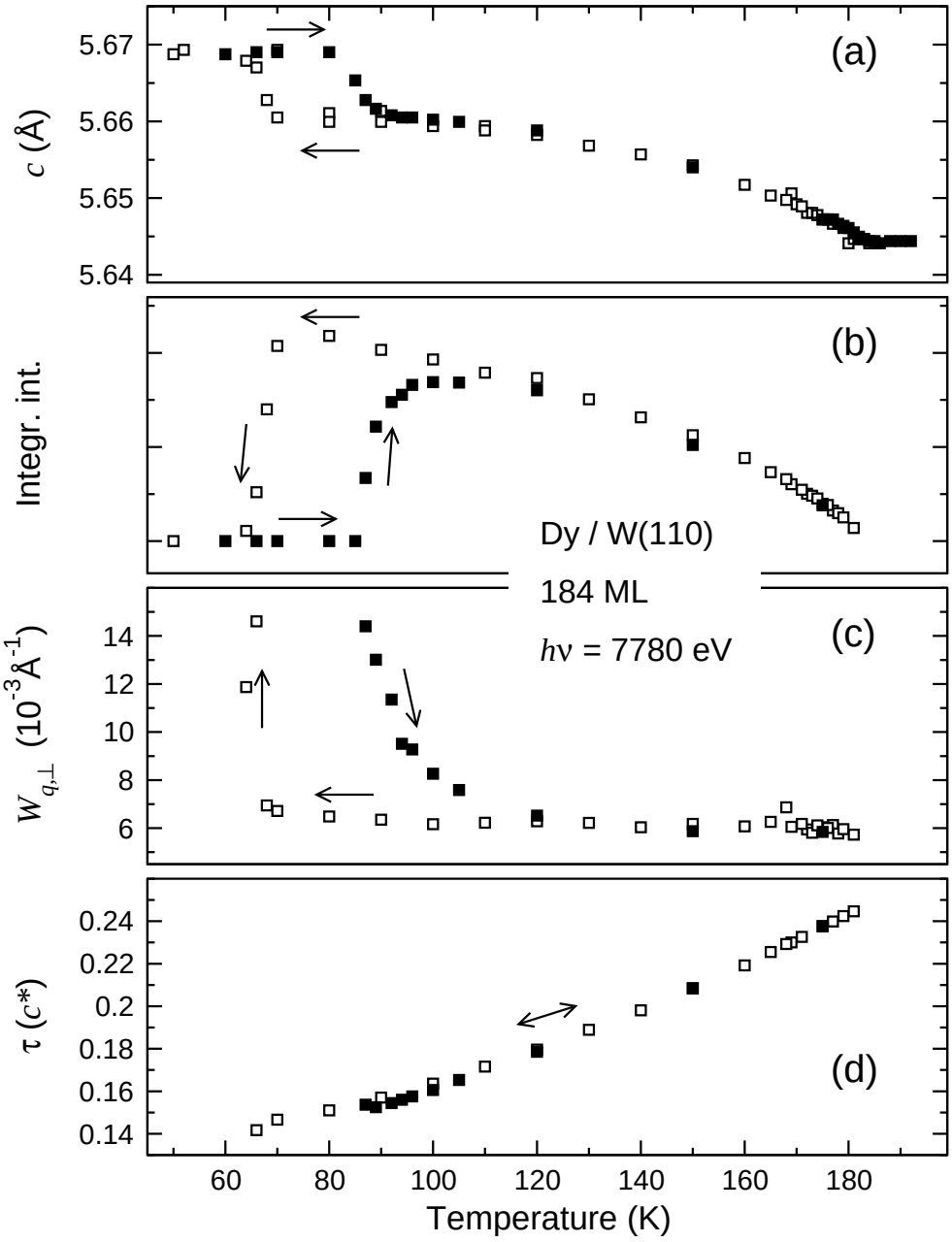

Figure 6.4: Parameters obtained from the (002) Bragg reflection and the (002$-\tau$) magnetic satellite as a function of temperature. The data were recorded at the Dy L_{III} resonance. The open squares represent data taken on the cooling path, the filled squares during warming up: (a) $c-$axis lattice parameter, (b) integrated intensity of the magnetic satellite, (c) width (HWHM) of the magnetic satellite along the crystallographic c axis, (d) magnetic modulation vector τ.

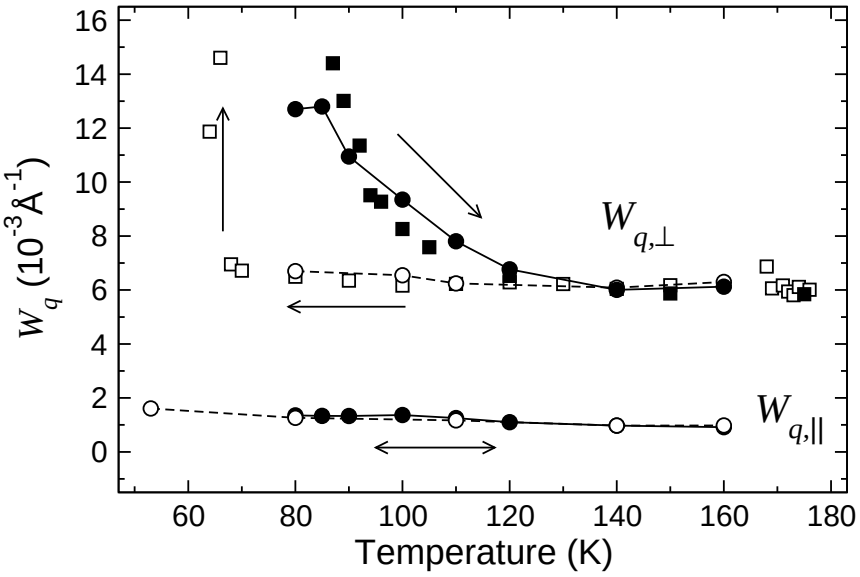

Figure 6.5: Width (HWHM) of the (002−τ) magnetic satellite as measured in the conventional x-ray region at 7780 eV (squares) and of the (000+τ) magnetic satellite measured at 1305 eV (circles), along the c axis, $W_{q,\perp}$, and within the basal plane, $W_{q,\|}$. The data were recorded during cooling (open symbols) and on the warming-up path (filled symbols) as indicated by the arrows.

magnetic-superstructure satellite drops in the same temperature interval. Upon heating (filled symbols), the $c-$axis parameter relaxes to its lower value with a hysteresis of about 20 K. With the same hysteresis, the magnetic satellite intensity grows upon heating indicating the reappearance of the helical-AFM phase, but it does not reach the value it exhibited during cooling. While the transition from the helical AFM to the FM phase occurs at about 68 K within a temperature interval of about 5 K, the helical structure develops on the way back even more delayed. Only about 35 K above its appearance temperature, the helical structure has fully recovered. Such a behavior had not been observed for bulk Dy or for Dy films with equal boundaries studied so far.

The behavior of the longitudinal width, $W_{q,\perp}$, of the magnetic satellite, displayed in figure 6.4 (c), further characterizes this delayed transition. On the cooling path, $W_{q,\perp}$ has a constant value that is given by the film thickness, indicating AFM order throughout the whole film. During the phase transition, the satellite gets broader in the same temperature interval in which the satellite intensity drops and disappears below about 66 K. Upon heating, the satellite reappears with nearly the same width it had right before it disappeared. Towards higher temperatures, the width decreases slowly, and it does not reach the value it had on the cooling path before the temperature is reached, where the satellite intensity has also fully recovered. Since $W_{q,\perp}$ is inversely proportional to the number of contributing atomic planes, its slow decrease upon heating is the signature of a helical domain growth along the surface normal. Whether the domain size grows laterally as well can not be

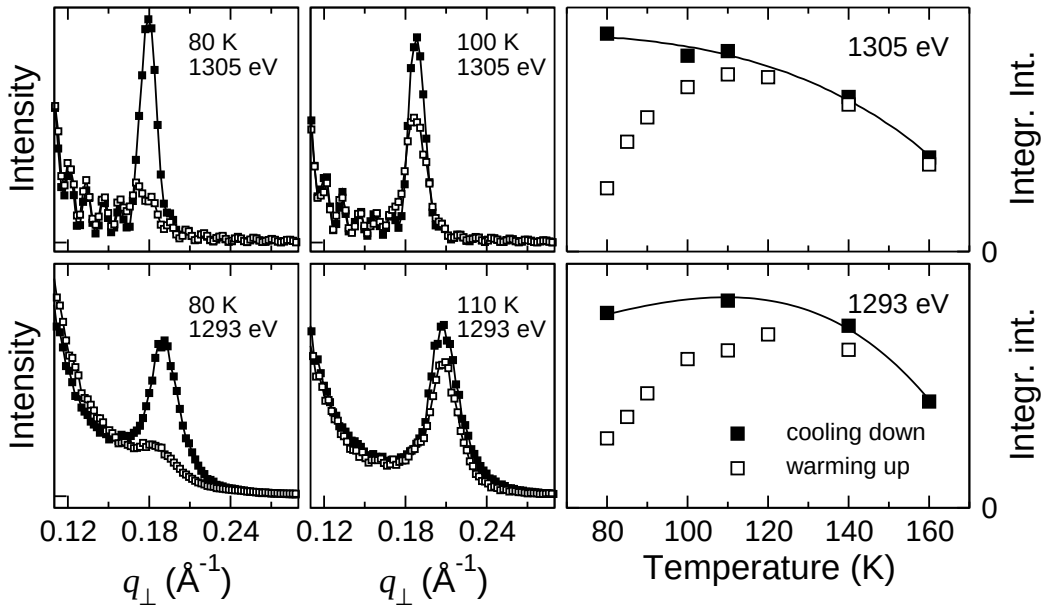

Figure 6.6: Specular reflectivity scans from an 180-ML Dy film. The data in the upper part were recorded at 1305 eV, probing the whole film, the data in the lower part were recorded near the resonance maximum (1293 eV) with a high surface sensitivity due to the strongly reduced photon penetration depth. The filled squares denote the spectra taken during cooling down, the open squares those taken during warming up. The respective rightmost panels show the satellite intensities, obtained on the cooling path (filled squares) and during warming up (open squares) for both photon energies.

answered from this experiment due to insufficient experimental resolution, which does not allow a statement about the magnetic in-plane coherence or the in-plane domain size of the magnetic structure. In any case, the FM phase is stabilized in one part of the film, while it is not in the other part. Considering the two inequivalent film boundaries, it is plausible to assume that one of them (or both, but with different strengths) stabilize the FM order. A suspicious candidate is the W/Dy interface, because the W(110) surface exhibits the same symmetry as the Dy basal plane in the FM phase as displayed schematically in figure 1.2. From the data presented so far, this assumption can not be proved, however, since details of the helix growth cannot be determined. This is due to the fact that the information obtained with conventional x-rays is averaged over the whole film. But the soft x-ray data allow a detailed and conclusive analysis as presented in the following.

6.3 Magnetic depth profile

An important open question so far is, whether the AFM domains grow in a laterally homogeneous way, as indicated by the behavior of the longitudinal width of the magnetic satellite. This can be answered using the higher momentum resolution easily obtainable

in the soft x-ray region due to the long wavelength, which leads to diffraction patterns distributed over a wide angular range. Figure 6.5 shows the results for the longitudinal width, $W_{q,\perp}$, and the width of the transverse scans, $W_{q,\parallel}$, measured at the L_{III} and M_V resonances. For $W_{q,\perp}$ the same behavior is found in both photon-energy regions. From the in-plane width, $W_{q,\parallel}$, no significant change of the in-plane magnetic coherence length of about 1000 Å can be observed, neither for different temperatures, nor between the cooling and the heating paths. This means that the growth of the helical domain can be considered as a quasi-one-dimensional process along the crystallographic c axis only, while it is laterally homogeneous at all temperatures. Note that the soft x-ray data were recorded at a photon energy of 1305 eV, where the probing depth is comparable to the film thickness, and that the obtained in-plane coherence is representative for the whole AFM-ordered parts of the film.

In order to obtain the magnetic profile along the c axis across the phase transition, temperature-dependent reflectivity measurements at various photon energies around the M_V absorption threshold were performed. The panels on the left side of figure 6.6 show reflectivity scans from a 180-ML Dy film grown on W(110). In each frame, the scans taken during cool-down are compared with those recorded on the warming-up path. The two lower frames show scans taken near the resonance maximum at 1293 eV, where the measurement is extremely surface sensitive with a probing depth of only about 30 Å along the surface normal. The strong absorption is reflected in the absence of the Kiessig fringes. The scans in the upper frames were taken at a higher energy of 1305 eV, where the x-rays penetrate the whole film, and Kiessig fringes appear in the reflectivity signal. Since the integrated scattered intensity is proportional to the number of scattering atomic planes, the satellite intensity contains information on the number of atomic layers in the helical phase in the respective probed volume. On the cooling path, the helical AFM structure is fully developed throughout the film and can be described exactly as shown in section 6.1. Upon heating, the magnetic-satellite shape is more complicated reflecting the temperature-dependent growth of the helical-AFM domain. The data were analyzed by fitting the background, ensuring a proper subtraction of the contributions due to charge scattering. The residual intensity of purely magnetic origin was then integrated; these integrated intensities in both directions of temperature variation and for both photon energies are presented on the rightmost panels of figure 6.6. The satellite intensity is proportional to the number of AFM layers. In addition to that, the scattered intensity is also affected by the temperature dependence of the magnetic order parameter and indirectly by the temperature dependence of the non-hysteretic magnetic modulation vector (figure 6.4(d)), which leads to a variation of the angle of observation, and thus to a changing optical path in the absorbing medium. The latter two dependences can be eliminated by normalizing the intensity on the heating path to that on the cooling path, which represents the magnetic order parameter of the whole film at the respective temperature. Thus, the remaining temperature-dependent variable is the number of layers in the AFM phase. The intensity ratio I_{up}/I_{down} of the integrated intensities during heating and cooling, respectively, is plotted as a function of temperature in the right panels of figure 6.7 for three selected photon energies. This ratio

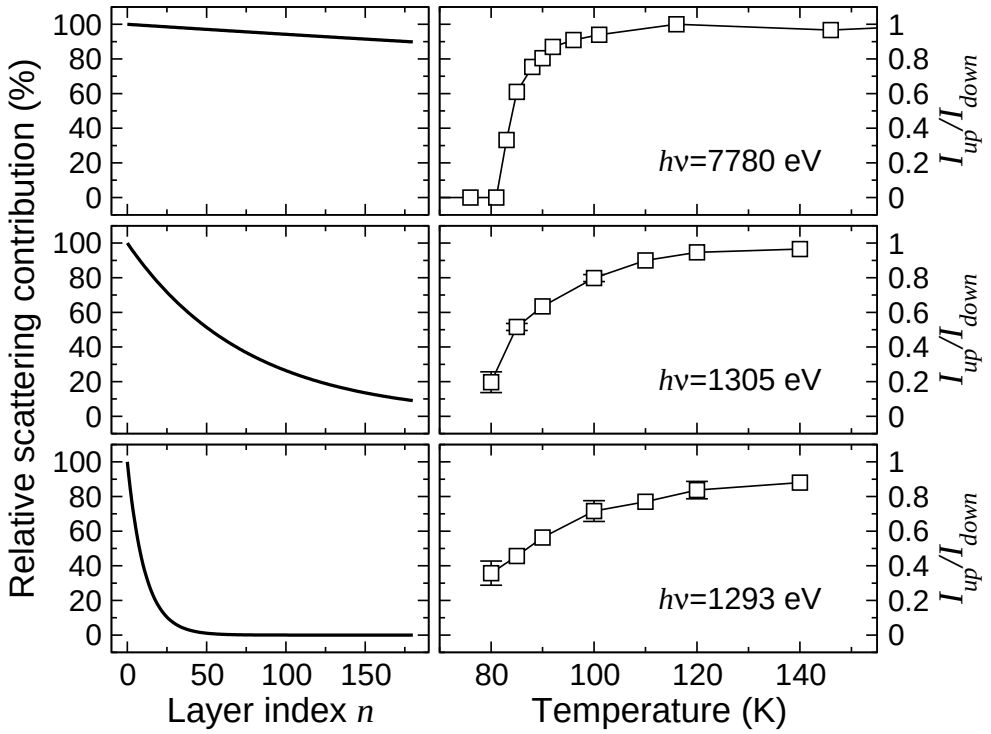

Figure 6.7: Left panels: relative contribution to the scattering signal as a function of the layer index n. The data were calculated for the different photon energies and for the scattering angle of the respective magnetic satellite using the β values of figure 6.2. While in the conventional x-ray region all layers contribute essentially with the same strengths, only intensity from the topmost layers can be detected near the M_V absorption threshold at 1293 eV. The right panels show the ratio of the intensities measured on the warming and cooling paths, I_{up}/I_{down}, respectively, for the three photon energies.

represents the relative number of layers contributing to the magnetic signal upon heating in the probed volume, which is determined by the photon-energy-dependent x-ray penetration depth. The corresponding information depth according to the photon absorption length is displayed in the left panels. In the conventional x-ray region (top), the contribution to the scattering signal is essentially the same (> 90 percent) for all atomic layers of the film. Thus, the data reflect the relative increase of the total number of AFM layers in the whole film upon heating. In contrast to that, the intensities measured in the soft x-ray region contain information only on the number of AFM-ordered layers up to a certain probing depth, and thus contain information on the magnetic depth profile. Extremely surface-sensitive data are obtained at 1293 eV photon energy. At low temperatures, the value of I_{up}/I_{down} for this photon energy is higher than for 1305 eV, where more layers of the film are probed. This result already indicates that the helical phase starts to grow near the surface.

From these data we can quantitatively determine the magnetic depth profile during

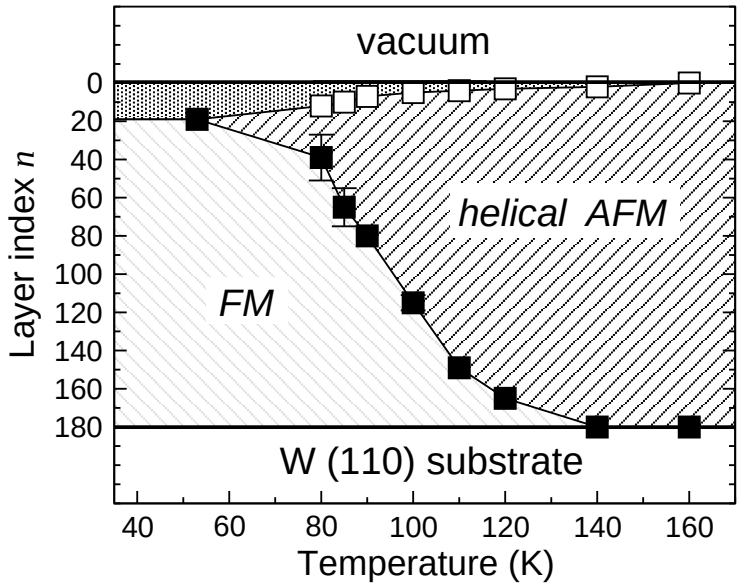

Figure 6.8: Magnetic depth-profile of a 180-ML Dy film during the first-order phase transition from the FM to the helical AFM phase. The data were calculated from the intensity ratio shown in the right panels of figure 6.7. The helical AFM phase develops essentially from the surface to the interface upon heating. In the surface area, there is a second AFM phase (gray shaded region) with a larger period length that persists into the FM phase.

the phase transition. The absorption of x-rays propagating through an absorbing medium follows Lambert-Beer's law, $I = I_0 e^{-\mu r}$, with I_0 being the initial intensity, r the path length, and $\mu = 4\pi\beta/\lambda$ the absorption coefficient. Accordingly, the intensity scattered from a partially AFM-ordered film, where the helix starts in layer n_1 counting from the surface and ends in layer n_2, is given by

$$I \propto \sum_{n=n_1}^{n_2} e^{-\mu n 2d/\sin\Theta}, \tag{6.1}$$

with the film thickness d and the scattering angle Θ.

Using this expression, the experimental ratio I_{up}/I_{down} can be simulated with the experimentally determined numbers for μ, using only n_1 and n_2 as free parameters. Upon cooling, $n_1 = 0$ and $n_2 = N - 1$, as the helix is fully developed across the whole film. Near the resonance maximum, the observed intensity does not depend much on n_2, and n_1 can be determined. Using this value for n_1 to simulate the data with larger probing depth gives n_2. Iterations of this procedure lead to a consistent description of I_{up}/I_{down} for all photon energies. The resulting development of the magnetic depth profile as a function of temperature is summarized in figure 6.8.

The AFM phase grows essentially from the surface towards the substrate over a temperature interval of about 50 K. This means that the FM phase is stabilized at the interface,

presumable due to uniaxial strain induced by the W(110) substrate as mentioned before.

The applied model describes the behavior of the helical AFM domain, while the remaining parts of the film are not characterized. From the behavior of the $c-$axis lattice parameter, however, the low-temperature magnetic structure can be readily identified as FM. Interestingly, the helical magnetic structure does not develop simply from one boundary to the other, but starts in the near-surface region and develops gradually in both directions. Thus, during the phase transition, the magnetic structure consists of three different domains. In the topmost domain, the magnetic structure deviates from FM alignment, even at low temperatures in the FM phase. This region can be assigned as a second helical-magnetic phase with a larger period length (gray shaded area in figure 6.8). Because the domain is very thin, the diffraction signal is very broad and only visible from the shape of the background intensity as measured close to the resonance maximum, where the experiment is more surface sensitive. This is illustrated in figure 6.9. The scans were taken at a photon energy of 1294.8 eV sensitive to an extended surface region of about 60 Å and show how the main peak evolves into a broad component during cool-down (left panel) and recovers when heated up (right panel). The change in the background between $q_\perp = 0.13\,\text{Å}^{-1}$ and $0.17\,\text{Å}^{-1}$ (open symbols), a measure for the surface helical phase, compared to the peak height of the main satellite (filled symbols) is shown in the respective inset. In both directions, there is a smooth transition from one to the other component in the near-surface region. Thus, the remaining helical phase at the surface is the starting point or the seed layer of the developing helical AFM structure.

Since the development of the helical magnetic structure can be characterized by small changes near the surface and a big change throughout the whole film, two sets of data, one at resonance and a second one recorded off-resonance provide sufficient information to reconstruct the magnetic structure and its development in the present case. But in general, the photon energies and thus the probing depths have to be found individually for each particular system.

The effect used to determine the depth profile is based on photon absorption, and thus allows the determination of structures along the surface normal combined with a certain in-plane information like the magnetic in-plane coherence. A combination of depth profiling and microdiffraction [142], would make a three-dimensional imaging of magnetic structures and magnetic domains possible. This may be an important tool in the future, since recent achievements in the field of multilayer magnetic devices with AFM layers have stimulated a renewed interest in AFM materials [152–154]. The variety of materials to which this method can be applied is huge, using e.g. the $M_{IV,V}$ absorption thresholds of other lanthanides [119] and actinides, or the comparably strong resonances at the $L_{II,III}$ thresholds of the 3d transition metals [110, 112]. Since we used only less than half of the available contrast in the absorption coefficient to achieve a sensitivity to the few topmost atomic layers in the present study, this method can be nicely applied also to compounds or dilute systems. In this context, one can think of AFM structures in correlated systems, or systems that exhibit charge or orbital ordering.

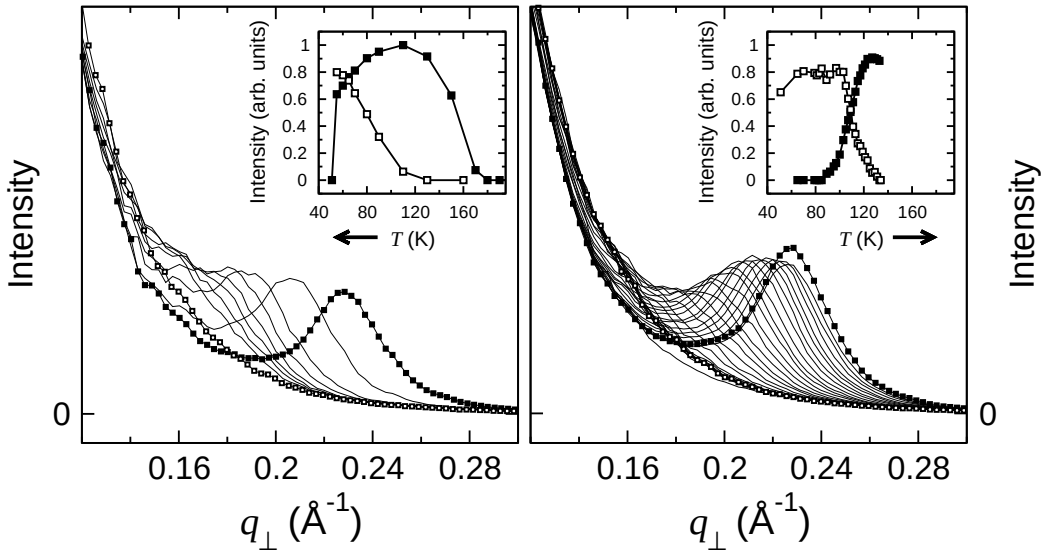

Figure 6.9: Detailed view of the change of the magnetic structure in the near-surface region during the first-order phase transition. The data were recorded from an 144-ML Dy film grown on W(110). The left side shows spectra during cooling down, the right side during warming up as indicated by the arrows. A smooth transition between two different helical magnetic phases is visible. The corresponding insets display the peak heights of the main satellites (filled symbols) and the changes in the background representing the second helical phase in the near-surface region (open symbols).